energies

MDPI

Article

Comparative Numerical and Experimental Analyses of Conical Solar Collector and Spot Fresnel Concentrator

Haedr Abdalha Mahmood Alsalame, Kang Kyeong Sik and Gwi Hyun Lee *

Department of Interdisciplinary Program in Smart Agriculture, Kangwon National University, Chuncheon 24341, Republic of Korea; alsalami@kangwon.ac.kr (H.A.M.A.); kks7524@kangwon.ac.kr (K.K.S.)
* Correspondence: ghlee@kangwon.ac.kr; Tel./Fax: +82-33-250-6495

Abstract: This paper aims to compare the thermal performances of the conical solar collector (CSC) system and the spot Fresnel lens system (SFL) using water and CuO nanofluid as the working fluids. The studied CFD models for both systems were validated using experimental data. At an optimal flow rate of 6 L/min, the SFL system showed higher optical and thermal performance in comparison with that of the CSC system. In the case of the SFL system, the availability of a greater amount of solar energy per unit collector area caused an increase in thermal energy. Moreover, in the case of the CSC system, the non-uniform distribution of solar flux on the absorber's outer surface leads to an increase in temperature gradient and heat losses. As a heating medium, the CuO nanofluid outperformed the water in terms of higher thermal conductivity and heat capacity. The average thermal efficiencies of 64.7% and 61.2% were achieved using SFL with and without CuO nanofluid, respectively, which were 2.4% and 0.5% higher than those of the CSC with and without nanofluid. CFD simulations show a 2.80% deviation for SFL and 2.92% for CSC, indicating acceptable accuracy compared to experimental data.

Keywords: collecting efficiency; conical solar concentrator; performance analysis; solar energy; Fresnel lens system; CFD

check for updates

Citation: Alsalame, H.A.M.; Sik, K.K.; Lee, G.H. Comparative Numerical and Experimental Analyses of Conical Solar Collector and Spot Fresnel Concentrator. *Energies* **2024**, *17*, 5437. https://doi.org/10.3390/en17215437

Academic Editors: George Kosmadakis, Chunrong Zhao and Jianyong Wang

Received: 26 August 2024
Revised: 8 October 2024
Accepted: 28 October 2024
Published: 31 October 2024

Copyright: © 2024 by the authors. Licensee MDPI, Basel, Switzerland. This article is an open access article distributed under the terms and conditions of the Creative Commons Attribution (CC BY) license (https://creativecommons.org/licenses/by/4.0/).

1. Introduction

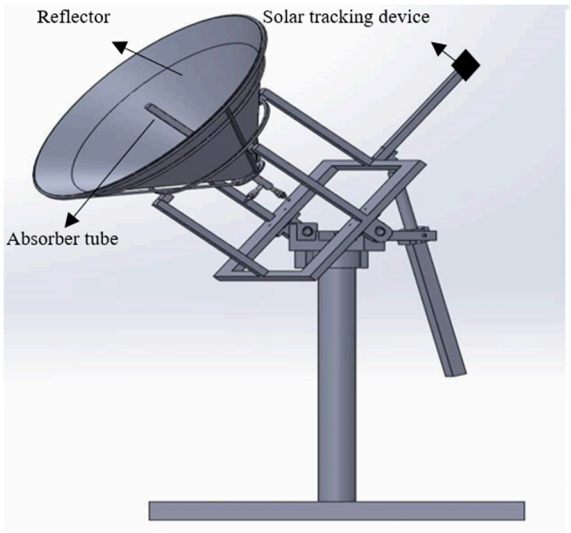
Concentrated solar energy is one of the most stable and promising renewable energy sources for applications that need higher temperatures. It is also a readily available energy source that can assist in mitigating the problems associated with environmental degradation brought on by the combustion of fossil fuels [1]. Mainly solar concentrators can be distinguished as refractive and reflective [2,3]. Both solar concentrators share the same goal of providing higher-temperature thermal output. Concentrated solar thermal collectors can be classified as dish Stirling, parabolic trough, conical solar concentrator, and central receiver systems. Over the past several years, due to high energy conversion efficiency, the Fresnel refraction system has been the preferred option for solar thermal applications [4,5]. The concentrated solar collectors are crucial when there is limited surface area [6]. Wassila Ajbar et al. [7] have discussed the various applications of parabolic trough collectors. They determined that electricity generation from steam power cycles with the help of concentrated solar flux is the most efficient way of utilizing solar energy potential. Xie et al. [8] reported the most recent advancements in Fresnel-based solar energy concentrating systems. They concluded that the Fresnel lens-based solar collector is an ideal choice for commercial solar energy applications because of its low weight, cost-effectiveness, and high-optical efficiency; however, high-precision sun tracking is crucial. El-Bakry et al. [9] analyzed and compared the performances of concentrated and nonconcentrated solar thermoelectric generators under controlled laboratory conditions. Power generation sees a remarkable increase of up to 82%. They suggested that the performance improvements achieved through absorbent layer deposition are particularly effective in concentrated

light environments. Xie et al. [10] conducted theoretical and experimental thermal performance assessments of the line focus Fresnel lens solar concentrator using various cavity receivers. They found that the solar collector's compact design, high energy density, and distribution of high flux incident on the receiver surface made the resultant integration noteworthy [11–13]. Lewandowski and Simms [14] evaluated and compared the thermal performance of the parabolic trough collectors and linear Fresnel lens collectors for water heating and steam production. The Fresnel lens collector is economically more viable than the parabolic trough collector when considering leveling energy cost; however, the total energy provided by both devices is almost equal. Xie et al. [15] developed a computer model in order to determine the ideal cavity receiver configuration and the temperature distribution for a point-focus Fresnel lens system. Quantitative and qualitative data from the numerical simulation and the experimental findings were agreed satisfactorily. Jeter [16,17] developed mathematical models for the estimation of the optical efficiency and the concentrated solar flux distribution in parabolic trough collectors by taking into account poor transmission, reflection, and absorption. Cheng et al. [18] used the finite volume and Monte Carlo ray-trace methods to simulate the complex photothermal conversion process of a parabolic trough solar collector. It is found that the proposed combination method may be used to investigate the processes of involute fluid dynamics and conjugate heat transfer in the entire receiver. Numerous numerical and experimental studies related to conical solar collectors, parabolic trough collectors, and Fresnel lens collectors have been published by different researchers, including Alsalame et al. [19–23]. However, to our best knowledge, no comparative numerical analysis of spot Fresnel lens (SFL) and conical solar collector (CSC) systems has been published so far. In this study, numerical models (using ANSYS FLUENT (2022 R2) software) for different components of CSC and SFC systems were developed and verified with the help of experimental results. Both systems were evaluated under similar geometrical, operating, and climatic conditions. This study used experimental data and computational results to determine the best solar energy collection system, and the working fluid based on the optical and thermal performances.

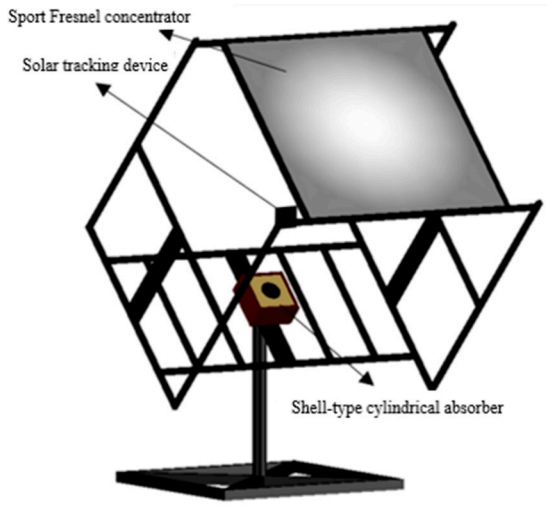
2. Materials and Method

2.1. Experimentation

The proposed CSC system consists of a conical concentrator that reflects the sunlight onto the absorber tube surface, while the SFL system consists of a Fresnel lens that converges the sunlight onto a copper shell-type cylindrical absorber, as shown in Figure 1.

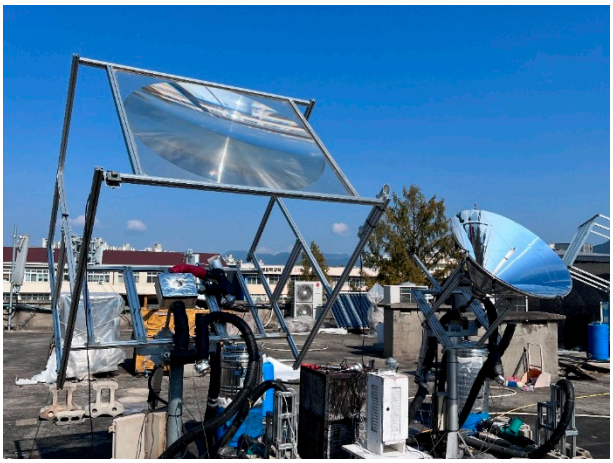


(**a**)



(**b**)

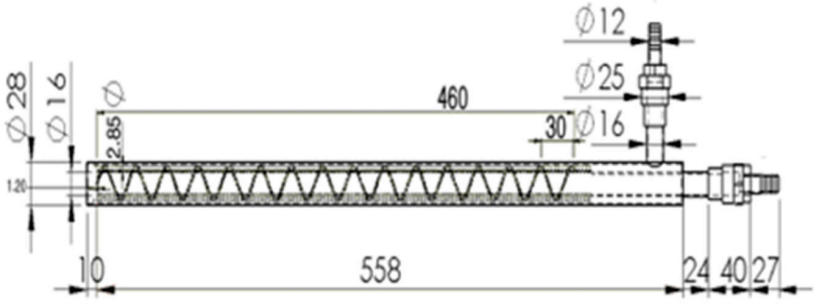
Figure 1. *Cont.*



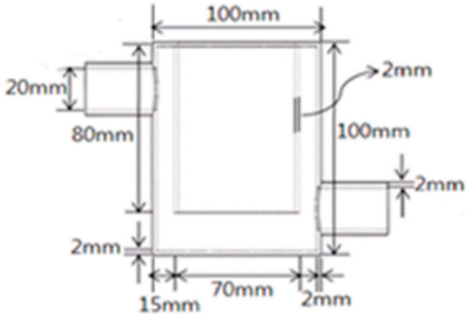
(**c**)

Figure 1. The solar thermal collector: (**a**) shows the conical solar collector (CSC); sub-figure (**b**) is the spot Fresnel lens concentrator (SFL); and sub-figure (**c**) shows the experimental setup of the reflector and absorber assembly for the CSC and SFL systems.

Both systems are equipped with heat storage tanks to store solar heat, each with a capacity of 40 L, an electric pump for circulation of heat transfer fluid or thermal medium, and a flow meter to measure the fluid flow rate. The solar heat extracted by the working fluid through absorbers was stored in a thermal storage tank. Both systems were mounted on a solar tracking system, which helped to maximize the utilization of available solar energy. To monitor the temperature of the working fluid, temperature sensors (PT 100 Ω) were used at the absorber's input and output. Both systems have a similar solar collecting surface area, and their other specifications are shown in Tables 1 and 2. The dimensions of the shell-type cylindrical absorber for the SFL system and the copper absorber tube for the CSC system are presented in Figure 2. The inserted coil inside the absorber is not hollow but solid and there is no fluid flow through it [21].

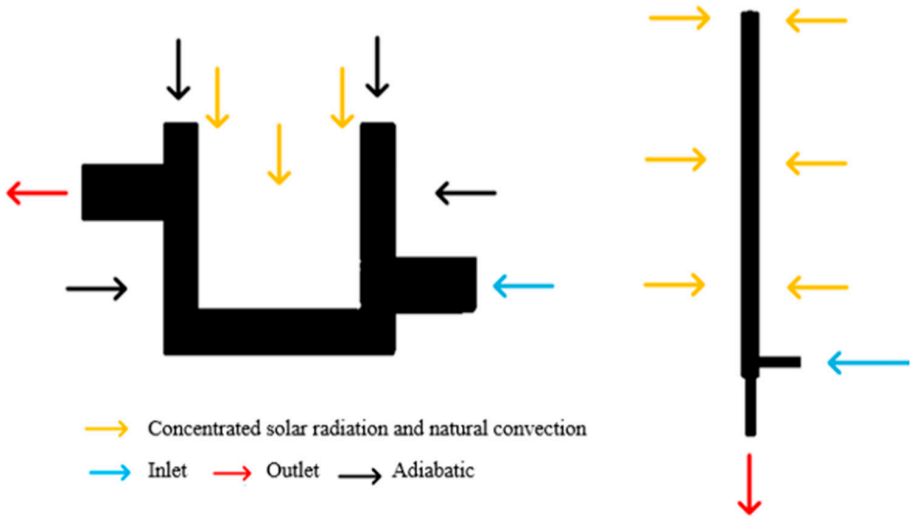


(**a**)

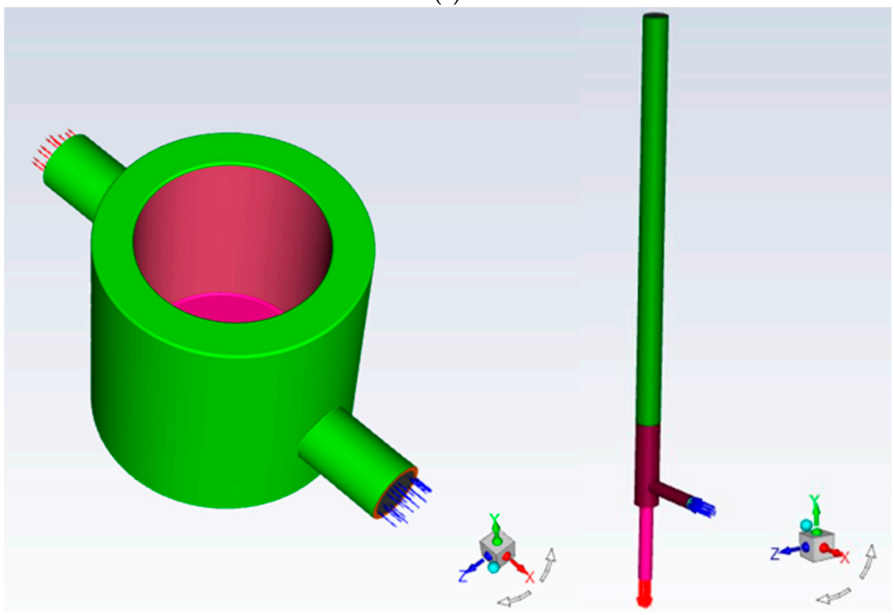


(**b**)

Figure 2. *Cont.*



(**c**)



(**d**)

Figure 2. The dimension details and boundary conditions of the collectors: (**a**) shows the coil absorber tube dimensions for the CSC; sub-figure (**b**) is the dimensions of the shell-type cylindrical collector for the SFL system [21]; sub-figure (**c**) shows the boundary conditions of the SFL's (**left**) and CSC's (**right**) absorbers; and sub-figure (**d**) is the 3D model of the SFL's (**left**) and CSC's (**right**) absorbers.

Table 1. Specifications of conical reflector.

Type	Specification
Material	Aluminum
Reflectivity (%)	92
Strength	H18
Concentration ratio (CR)	17.07
Concentrating surface area	0.80 m^2

Table 2. Fresnel lens specifications.

Type	Specification
Type	CPV
Texture	PMMA
Concentrating surface area	0.82 m^2
Pitch	0.5 mm
Concentration ratio (CR)	470X

For both systems, CuO nanofluid and water were utilized as the heat transfer medium, and the heat collecting efficiency of each system was examined for a period of 300 min. Experiments were conducted on the same day at the same flow rate; the flow rates used were 2, 4, and 6 L/min. The properties of the CuO nanofluid were calculated according to our previous study [24]. Briefly, the concentration of the CuO nanofluids was 0.5 weight percent in primary distilled water. To improve the dispersion stability, the surfactant Arabic Gum (GA) along with nanoparticles was added to distilled water while stirring, and later, the whole solution was sonicated using an ultrasonicator. Using a thermal characteristic analyzer, the produced nanofluid was analyzed multiple times; the nanofluid with the highest thermal conductivity was employed in the experiment. Comparative performance analyses were conducted for the duration of 300 min from 10:00 am to 3:00 pm. Compared to the earlier study of [24], the solar radiation was captured using a two-axis tracking platform.

2.2. Energy Performance Analysis

The heat collection efficiency for both systems was examined under similar operating and climatic conditions. The energy performance analysis of the aforementioned solar collectors was performed at three different flow rates: 2 L/min, 4 L/min, and 6 L/min. The thermal energy output (Q) can be calculated as follows [24]:

$$Q = mC_p(T_o - T_i) \tag{1}$$

where C_p and Q are the specific heat and flow rate, respectively, of the heat transfer fluid. T_i and T_o are the fluid inlet and outlet temperatures.

The heat collecting efficiency (η) was calculated using Equation (2) to examine the efficiency of the two systems as follows:

$$\eta = \frac{Q}{Al} \tag{2}$$

where l and η are the beam radiation and thermal efficiency, respectively, and the collector area is A.

The temperature variation across the absorber of each system is evaluated by using the CFD method. In the transient state, both systems exhibit different thermal behavior due to differences in geometry and thermal characteristics. For instance, different amounts of heat losses from the collecting absorber to the atmosphere occur because of differences in the heat transfer coefficients.

2.2.1. Numerical Analysis

The analyses were performed to observe temperature variation at different fluid flows. For simulation, ANSYS FLUENT software (2022 R2 ANSYS Inc., Kirkland, WA, USA) was used.

For simulation, the absorber models were created using grids which were generated using a meshing tool, and the grids were calculated using the finite volume method. The thermal performance analysis using heat transfer equations was performed under almost similar conditions aligned with the actual experiment environment. The heat transfer phenomenon was analyzed using the following equations:

Mass conservation equation:

$$\frac{\partial \rho}{\partial t} + \nabla \cdot \left(\rho \vec{v} \right) = S_m \tag{3}$$

where $\frac{\partial \rho}{\partial t}$ and $\nabla \cdot \left(\rho \vec{v} \right)$ are the rate of change in density with time and divergence of mass flow, respectively, and the mass change rate is S_m.

Reynolds number equation:

$$Re = \frac{\rho V L}{\mu} \tag{4}$$

where ρ is the fluid density, V is the flow velocity, L is the characteristic length, and μ is the dynamic viscosity of the fluid. Reynolds numbers against the 2–6 L/min have been reported as follows:

2 L/min = 1580
4 L/min=3300
6 L/min = 4800

For Re < 2000, the flow is classified as laminar. In the range 2900 < Re < 4000, the flow is in the transition region, while for Re > 4000, the flow becomes fully turbulent.

Momentum equation:

$$\rho(u\frac{\partial u}{\partial x} + v\frac{\partial u}{\partial y} + \omega\frac{\partial u}{\partial z}) = -\frac{\partial p}{\partial x} + (\mu + \mu_t)\left\{ \frac{\partial^2 u}{\partial x^2} + \frac{\partial^2 u}{\partial y^2} + \frac{\partial^2 U}{\partial z^2} \right\} \tag{5}$$

$$\rho(u\frac{\partial v}{\partial x} + v\frac{\partial v}{\partial y} + \omega\frac{\partial v}{\partial z}) = -\frac{\partial p}{\partial y} + (\mu + \mu_t)\left\{ \frac{\partial^2 v}{\partial x^2} + \frac{\partial^2 v}{\partial y^2} + \frac{\partial^2 v}{\partial z^2} \right\} - pg_y \tag{6}$$

$$\rho(u\frac{\partial \omega}{\partial x} + v\frac{\partial \omega}{\partial y} + \omega\frac{\partial \omega}{\partial z}) = -\frac{\partial p}{\partial z} + (\mu + \mu_t)\left\{ \frac{\partial^2 \omega}{\partial x^2} + \frac{\partial^2 \omega}{\partial y^2} + \frac{\partial^2 \omega}{\partial z^2} \right\} \tag{7}$$

Energy equation:

$$\rho c_p \frac{\partial T}{\partial t} + \rho c_p \nabla \cdot (u_i T) = -\nabla \rho + \left[k + \frac{c_p \mu_t}{P_{r_t}} \right] \nabla^2 T + (\mu + \mu_t) \frac{\partial u_i}{\partial x_j} \left\{ \frac{\partial u_i}{\partial x_j} + \frac{\partial u_j}{\partial x_i} + \frac{2}{3} \frac{\partial u_i}{\partial x_i} \delta_{ij} \right\} \tag{8}$$

Transport equations for standard *k*–ε model:

Representative examples include the *k*–ε model, the k–ω model, Large Eddy Simulation (LES), and Direct Numerical Simulation (DNS), and these models can be selected in various ways depending on various conditions including the Reynolds number. In this simulation, the standard *k*–ε model was used for simple turbulence of absorber analysis. The standard *k*–ε model is considered by low computational cost. So efficient and reliable is economical for analysis. In addition, the flow velocity is not excessively high, and the geometric complexity is simple. The model was chosen to avoid excessively high computational costs compared to the simple flow covered in this experiment.

k—equation equation:

$$\frac{\partial}{\partial t}(\rho k) + \frac{\partial u}{\partial x_i}(\rho k u_i) = \frac{\partial}{\partial x_j}\left[\left(\mu + \frac{\mu_t}{\sigma_k} \right) \frac{\partial k}{\partial x_j} \right] + P_k + -\rho\epsilon \tag{9}$$

ε—equation:

$$\frac{\partial}{\partial t}(\rho \epsilon) + \frac{\partial u}{\partial x_i}(\rho \epsilon u_i) = \frac{\partial}{\partial x_j}\left[\left(\mu + \frac{\mu_t}{\sigma_\epsilon} \right) \frac{\partial k}{\partial x_j} \right] + C_{1\epsilon}\frac{\epsilon}{k}(P_k + C_{3\epsilon}) - C_{2\epsilon}\rho\frac{\epsilon^2}{k} \tag{10}$$

here the turbulent viscosity is modeled as:

$$\mu_t = \rho C_\mu \frac{k^2}{\epsilon} \tag{11}$$

and

$$P_k = \mu_t S^2 \tag{12}$$

S is the modulus of the mean rate-of-strain tensor, defined as:

$$S = \sqrt{2 S_{ij} \, S_{ij}} \tag{13}$$

and $C_{1\epsilon} = 1.44$, $C_{2\epsilon} = 1.92$ $C_\mu = 0.09$ $\sigma_k = 1.0$ and $\sigma_\epsilon = 1.3$.

For the calculation of the natural heat transfer coefficient, we have used the following correlation [25,26]:

$$h_c = 10.45 - v + 10\, v^{1/2} \tag{14}$$

where h_c is the heat transfer coefficient and v is the relative speed between the object surface and air (m/s).

In steady state conditions, ANSYS FLUENT software observes the thermal and fluid fluctuation of every volume by applying the above equations in the FVM (finite volume method). FVM is a numerical technique for solving partial differential equations by dividing the computational domain into discrete control volumes or cells. FVM focuses on the conservation of flux over the control volume surfaces and on the integral form of the governing equations.

2.2.2. Meshing and Boundary Conditions

Both absorbers were meshed with poly-hexcore to curved and planar surfaces. Poly-hexcore mesh provides high-stability, lower RAM usage, and faster analysis time than other mesh shapes. Although the amount of grid cells for the shell-type absorber was twice than that of the conical, it seems improbable to meaningfully impact the simulation. The aspect ratio, representing the ratio of the longest to shortest length from a grid, was close to 0 for both absorbers, which indicates grid uniformity. The orthogonal quality is expressed between 0 and 1; therefore, the closer to 1, the higher the uniformity, indicating better grid quality. It meets the required criteria by showing a high mean value close to 1 and a minimum value exceeding 0.01. Skewness, which represents the fineness of the grid in terms of asymmetry, showed maximum values of between 0.5 and 0.7 in this model, which is an appropriate value for analysis. Table 3 shows a detailed description of the mesh status for the designed absorber models.

Table 3. CFD detailed description table.

	Shell-Type Absorber	**Conical Type Absorber**
Type of mesh	Poly-hexcore	Poly-hexcore
Number of elements	1,231,606	604,646
Maximum aspect ratio	1.23630×10	5.04985×10
Minimum orthogonal quality	2.10455×10^{-1}	9.90534×10^{-2}
Average orthogonal quality	0.93095659	0.93080005
Maximum skewness	0.53255203	0.7377065

The model flow chart for assessing absorber performance is shown in Figure 3. The grids of the two geometric models are as shown in Figures 4 and 5.

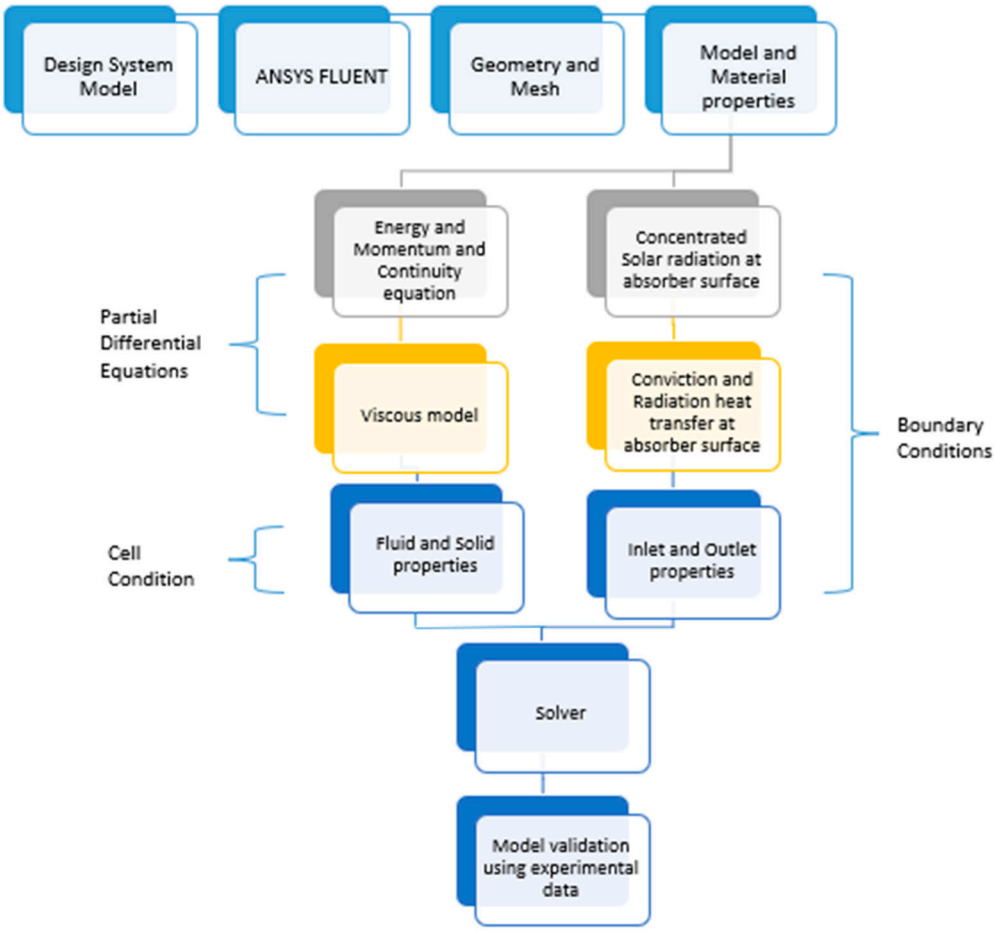


Figure 3. Schematic flow chart of solar heat absorber CFD simulation.

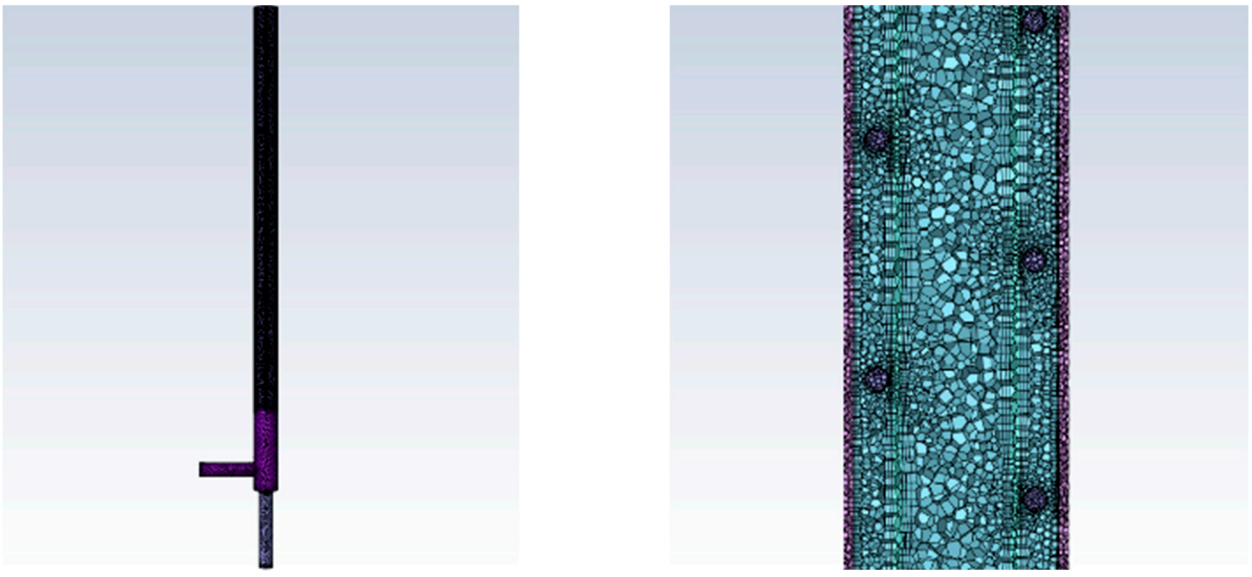


Figure 4. Geometry design and grid of absorber tube collector.

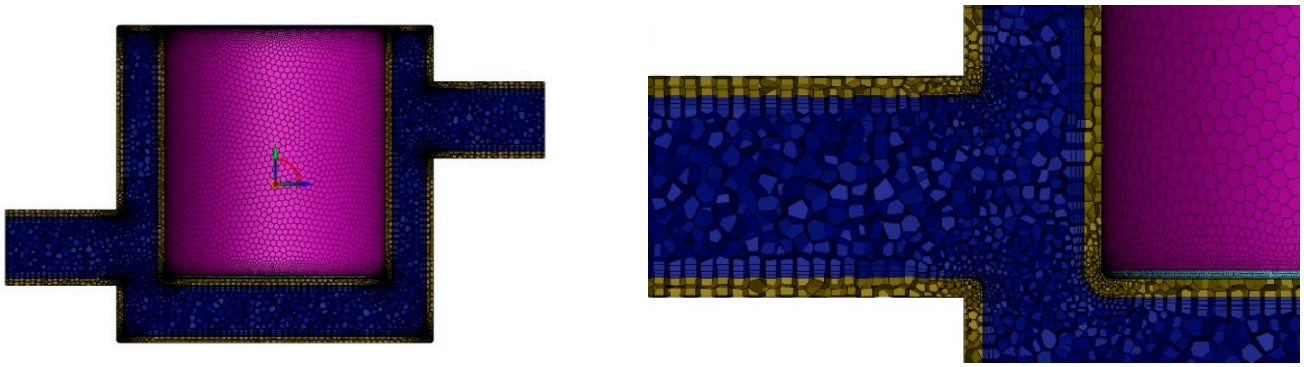


Figure 5. Geometry design and grid of shell-type absorber collector.

The boundary conditions of the analysis were set as similar as possible to the experimental conditions. Direct solar radiation in 800 W/m^2, which is almost similar to the experimental condition, was set according to the concentration ratio (CR) as boundary conditions to the absorption section. In addition, insulation and natural convection were applied as boundary conditions to other free walls. Table 4 shows the input data for the simulation which includes boundary conditions, material used, and the analysis conditions.

Table 4. Boundary conditions.

	Shell-Type Absorber	Conical Type Absorber
Analysis condition	Steady state	
Material	Copper	
Area of conical solar collector (m^2)	0.8	
Absorber area (m^2)	3.63168×10^{-3}	4.13433×10^{-2}
Inlet temperature (°C)	24	
Ambient temperature (°C)	21	
Beam radiation (W/m^2)	800	

3. Results and Discussions

The average efficiency of the CSC and SFL systems was compared using water and CuO nanofluid as working fluids at fixed flow rates of 2, 4, and 6 L/min. Experiments for aforesaid systems were conducted under almost similar weather conditions. The average daily variations in solar radiation, ambient temperature, and wind speed are depicted in Figure 6.

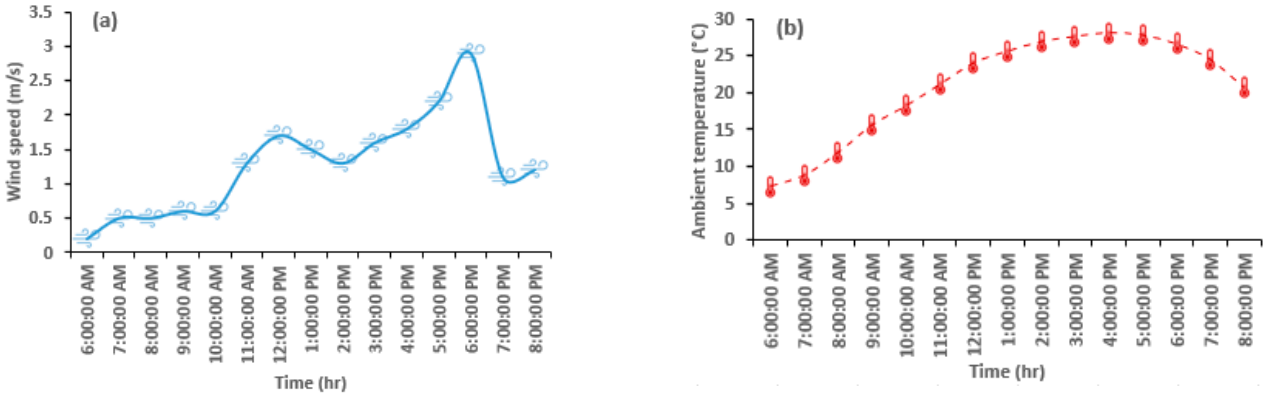


Figure 6. *Cont.*

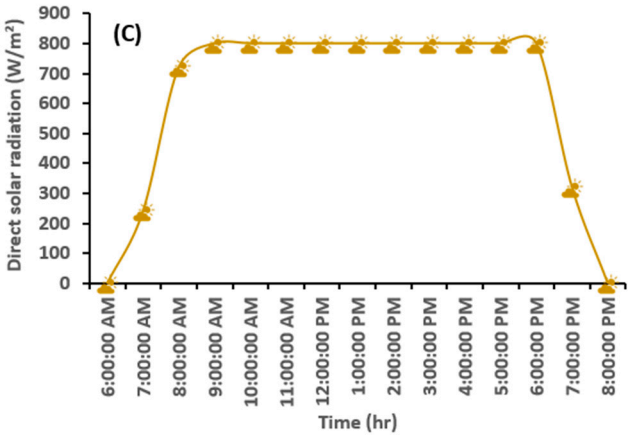


Figure 6. Daily variation in weather parameters: (**a**) wind speed; sub-figure (**b**) ambient temperature; and sub-figure (**c**) direct solar radiation.

Figure 7 shows the variations in average heat collection efficiency with time for the SFL and CSC systems using water and CuO nanofluids as working fluids at a flow rate of 2 L/min. The heat collection efficiency of the SFL system using CuO nanofluid was higher compared to that of the CSC system while using both nanofluid and water. When considering the results of the preliminary experiment, the thermal efficiency of the SFL while using the nanofluid and water was 56.6% and 54.8%, respectively. For the CSC system, the thermal efficiency was 54.7% and 52.6% while using nanofluid and water, respectively. In addition, the total efficiency improved by around 2% by using the nanofluid compared to the systems using water. This can be explained by the fact that nanofluid has higher thermal conductivity compared to water.

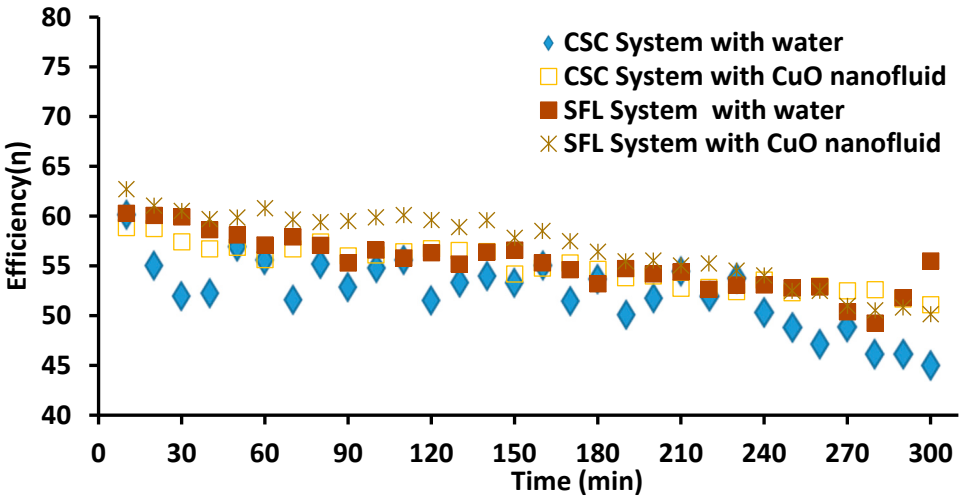


Figure 7. The daily variation in thermal efficiency at a flow rate of 2 L/min.

Figure 8 shows the experiment results of the average heat collection efficiency for the CSC and SFL systems with the time at a fixed flow rate of 4 L/min. A significant increase in thermal efficiency can be observed for both systems by increasing the flow rate up to 4 L/min. The thermal efficiency for the SFL system was 62.7% and 60.3% while using nanofluid and water, respectively. The thermal efficiency of the CSC system was 61.5% and 59.8% while using nanofluid and water, respectively.

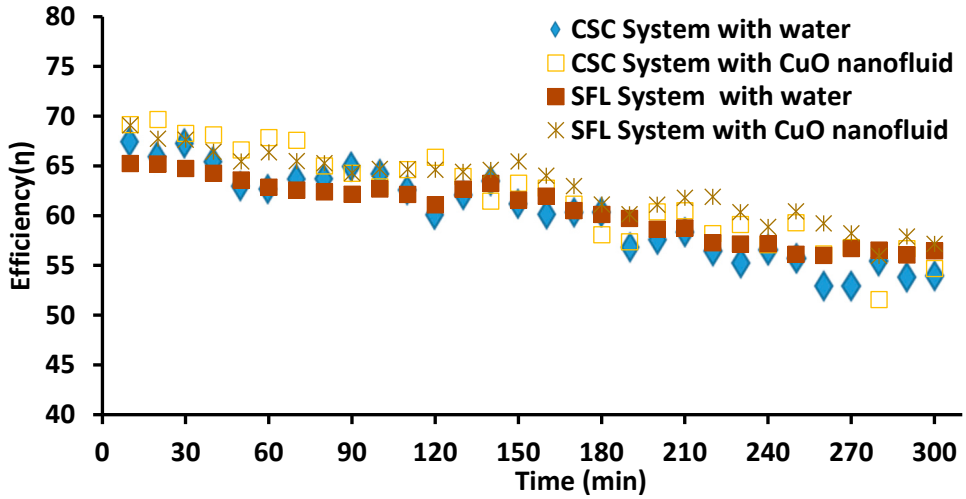


Figure 8. The daily variation in thermal efficiency at a flow rate of 4 L/min.

Figure 9 shows the changes in average heat collection efficiency with the time for the SFL and CSC systems using water and CuO nanofluids at a flow rate of 6 L/min. A slight increase in thermal efficiency can be observed for both systems by increasing the flow rate to 6 L/min. The heat collection efficiency of the SFL system using CuO nanofluid was higher compared to the CSC system while using nanofluid and water. The thermal efficiency of the SFL was 64.8% and 61.2% while using nanofluid and water, respectively. For the CSC system, the thermal efficiency was 62.3% and 60.7% while using the nanofluid and water, respectively. In addition, the total efficiency improved by around 2% by using the nanofluid compared to the same systems with water.

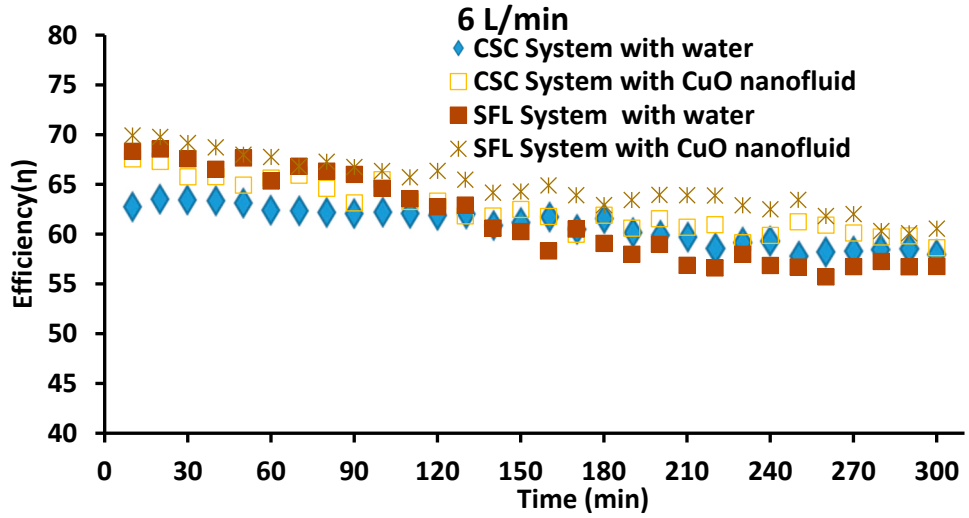


Figure 9. The daily variation in thermal efficiency at a flow rate of 6 L/min.

The steady state of the average thermal collection efficiency for the flow rate of 2 L/min with respect to the temperature difference between the fluid at the inlet and ambient air is shown in Figure 10. Under steady-state conditions, the thermal collection efficiency of the SFL system using CuO nanofluid was higher compared to the SFL system with water, and the CSC system with both nanofluid and water. Furthermore, the achieved steady-state thermal efficiency for the SFL system with nanofluid and water is 56.6% and 54.8%, respectively. For the CSC system, these values reduced to 54.7% and 52.6%, respectively. It was determined that extra heat loss occurred at a flow rate of 2 L/min because of the higher temperature difference between the absorber surface and the ambient air.

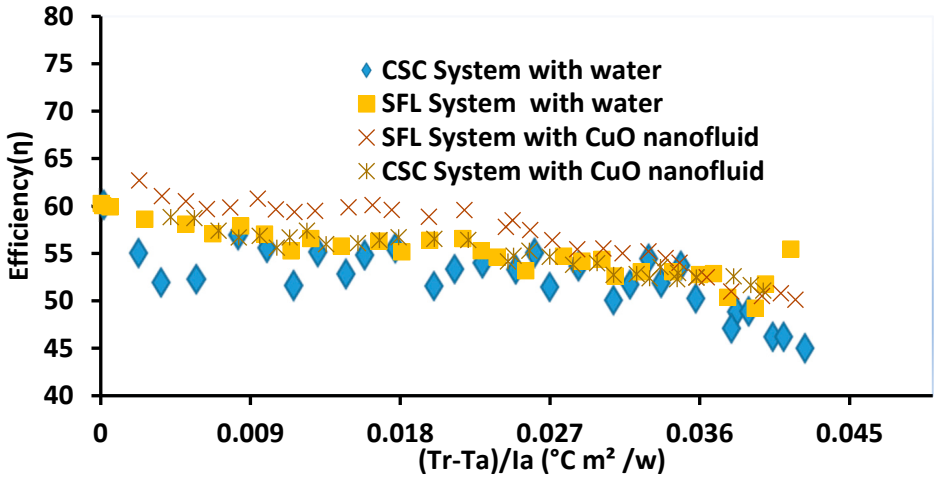


Figure 10. Correlation between efficiency and (Ti − Ta)/Ia parameter at flow rates of 2 L/min.

In addition, the steady state of the average collecting thermal efficiency for the flow rate of 4 L/min with respect to (Ti − Ta)/Ia factor is shown in Figure 11. At a flow rate of 4 L/min, the SFL system with CuO nanofluid showed the highest thermal efficiency compared to other studied solar systems, while the CSC system with water had the lowest thermal efficiency. Furthermore, the thermal efficiency with water and nanofluid for the SFL system is 62.7% and 60.3%, respectively, and the values for the CSC system are 61.5% and 59.8%, respectively. For the flow rate of 4 L/min, an enhancement of the thermal efficiency was observed on an average of 6.3% compared to the 2 L/min.

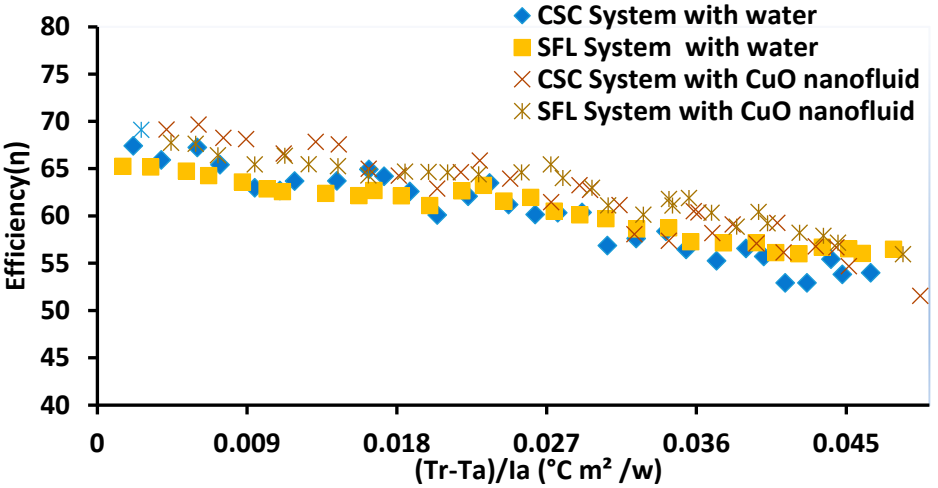


Figure 11. Correlation between efficiency and (Ti − Ta)/Ia parameter at flow rates of 4 L/min.

In addition, the steady state of the average thermal efficiency at a flow rate of 6 L/min against the (Ti − Ta)/Ia factor is shown in Figure 12. The CSC and SFL systems demonstrate optimal efficiency and a decrease in heat loss relative to lower flow rates. In the CSC system, the efficiency reaches 60.7% with water and 62.3% with nanofluid, representing a significant enhancement compared to the efficiencies at 2 L/min and 4 L/min. Similarly, in the SFL system, the efficiency peaks at 61.2% with water and 64.8% with nanofluid, showing consistent improvement over lower flow rates. The higher flow rate of 6 L/min improves heat transfer by reducing the temperature difference between the collector and the ambient temperature, which in turn reduces heat losses. At lower flow rates, such as 2 L/min and 4 L/min, the systems experience greater heat loss due to slower fluid movement, which allows for more heat dissipation to the ambient air. The nanofluid also contributes to reducing heat loss by enhancing the thermal conductivity of the working fluid, leading to

better retention of absorbed solar energy. Overall, the 6 L/min flow rate offers a balance between maximizing heat transfer and minimizing heat loss, especially in the SFL system where the performance gains are most pronounced.

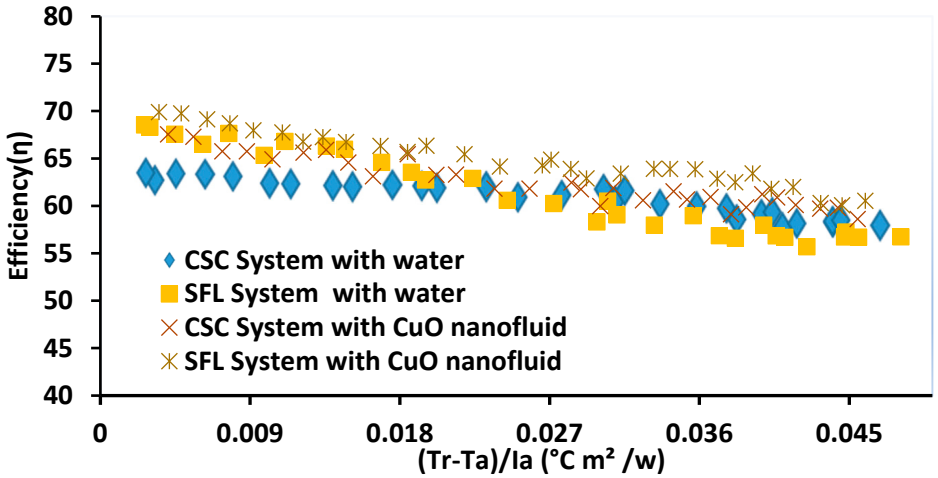
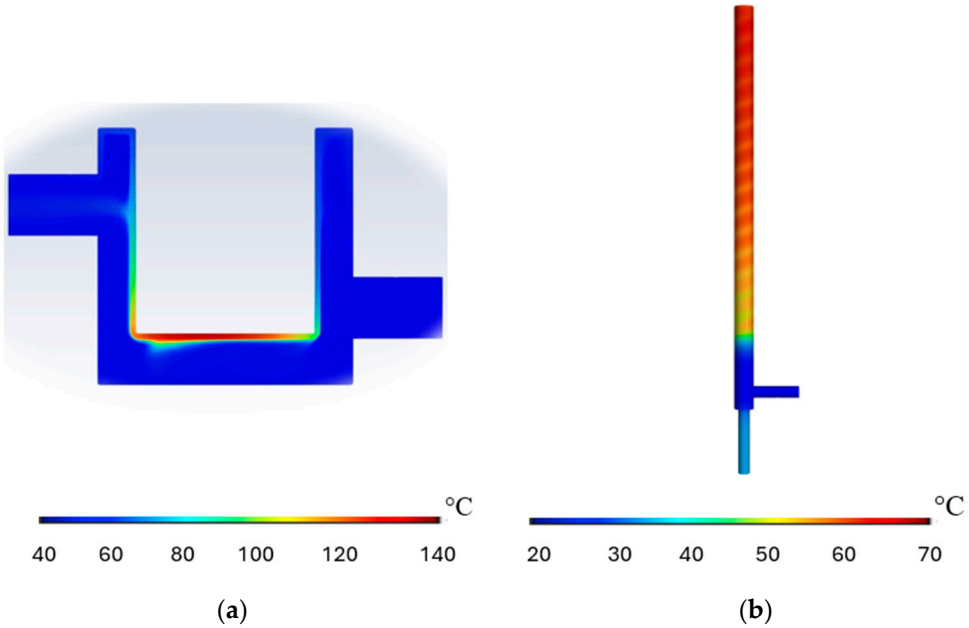


Figure 12. Correlation between efficiency and (Ti − Ta)/Ia parameter at flow rates of 6 L/min.

Model Validation Using CFD

Figure 13 shows the temperature distribution on the absorbers' surfaces as a result of concentrated solar radiation while using water at a flow rate of 6 L/min. Figure 14a,b show the comparison of absorber outlet temperature using CFD findings and experiment data.



(**a**) (**b**)

Figure 13. Absorbers contour through CFD at 6 l/min using water as working fluid: (**a**) shell-type cylindrical collector; (**b**) absorber tube.

The overall accuracy of the CFD simulations is verified in relation to experimental data. In the case of the spot Fresnel lenses, the difference between CFD findings and experimental data is about 2.80%, which shows a moderate average deviation. Similarly, in the case of the conical solar concentrator, the difference is about 2.92%, which supports the level of accuracy by displaying the discrepancies within acceptable limits. This demonstrates that the CFD model's accuracy is satisfactory across both studies, with differences that are reasonably consistent yet offer areas for development. Several factors contribute

to the differences between the CFD predictions and the actual experimental data. One probable explanation is that the CFD model has intrinsic limitations, such as simplifying assumptions that may not fully convey the real-world complexity of the experimental setups [27]. Furthermore, changes in measurement accuracy and experimental design could explain the observed accuracies [28]. For example, differences in the positioning or calibration of temperature sensors may result in inconsistencies. Variations in material qualities, ambient circumstances, or model resolution may also affect the accuracy of CFD simulations [29]. Addressing these issues through enhanced model calibration, finer mesh resolution, and greater experimental control may improve the alignment of CFD predictions and the experimental data.

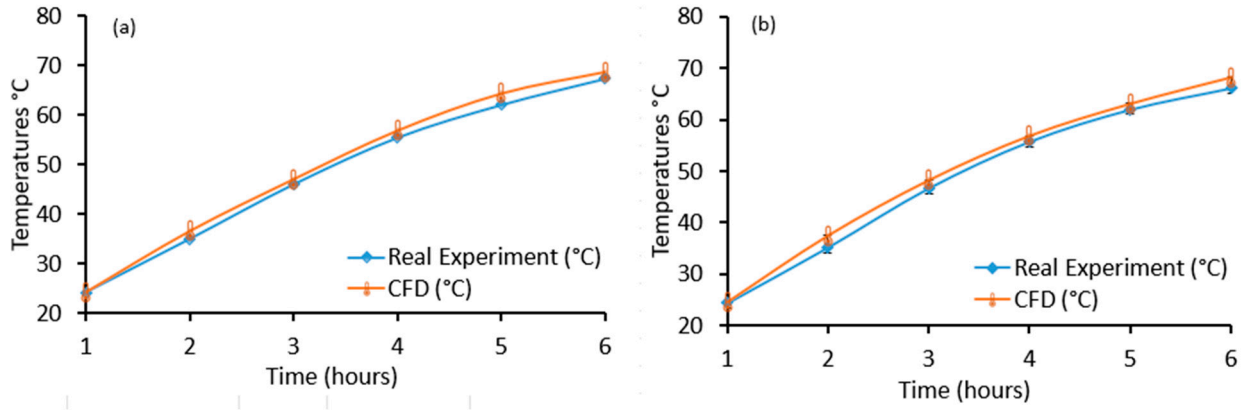


Figure 14. Model validation using CFD at 6 l/min using water as working fluid: (**a**) spot Fresnel lens system; (**b**) conical solar concentrator system.

4. Conclusions

To assess the efficiency of the CSC and SFL systems, a comparative study has been performed where CuO nanofluid and water were used as heat transfer fluids at varying flow rates of 2, 3, and 6 L/min. The total thermal collection efficiency of the SFL system using CuO nanofluid at 6L/min was 64.8%, and 62.3% for the CSC system with CuO nanofluid. While using water as a heating medium, the achieved thermal efficiency for the SFL and CSC systems were 61.2% and 60.7%, respectively. Due to higher thermal conductivity, the CuO nanofluid outperformed water as a heating medium. In the case of the best flow rate, 6 L/min showed the highest efficiency compared to 4 and 2 L/min, this is because the 6 L/min has a higher value of heat transfer coefficient in comparison with the aforesaid flow rates. Hence, the difference in thermal efficiency was significant. The SFL system has higher thermal efficiency in comparison with the CSC system which is around an average of 2% in all cases; this is because the surface area of the absorber pipe for the CSC system is larger than the shallow absorber for the SFL system, which results in more heat losses. The suggested SFL and CSC models for simulation analysis were further validated using experimental data. It is concluded that the measured data and the numerical findings depicted great harmony. The ambient air velocity had a significant impact on the actual measured absorber temperature, which could have contributed to the discrepancy between the predicted and actual findings. The overall accuracy of the CFD models is confirmed to be 2.80% for the SFL system and 2.92% for the CSC system, demonstrating moderate variances within the acceptable ranges. For future studies, it is suggested that introducing insulated glass covers over the absorbers could improve the efficiency of both systems by reducing excessive heat loss.

Author Contributions: Conceptualization, H.A.M.A.; methodology, K.K.S.; software, K.K.S.; validation, H.A.M.A. and K.K.S.; formal analysis, H.A.M.A.; investigation, H.A.M.A.; resources, H.A.M.A.; data curation, H.A.M.A.; writing—original draft preparation, H.A.M.A.; writing—review and edit-

ing, H.A.M.A.; visualization, G.H.L.; supervision, G.H.L.; project administration, G.H.L.; funding acquisition, G.H.L. All authors have read and agreed to the published version of the manuscript.

Funding: This work was supported by the National Research Foundation of Korea (NRF), grant funded by the Korea government (MSIT) (No.2022R1F1A1062793).

Data Availability Statement: The original contributions presented in this study are included in the article. Further inquiries can be directed to the corresponding author.

Conflicts of Interest: The authors declare no conflicts of interest.

Nomenclature

A	collector area (m^2)
c_p	specific heat of the water in the tank (J/kg·°C)
C_p	specific heat (J/kg·°C)
$C\mu$, $C_{1\varepsilon}$, $C_{2\varepsilon}$, $C_{3\varepsilon}$	coefficients in the turbulence model
$C_{1\varepsilon}$	$\kappa-\varepsilon$ turbulence model constant
d	characteristic length (m)
g	gravity (m/s^2)
h_c	heat transfer coefficient ($kCal/m^2h$ °C)
Re	Reynolds number
k	turbulent kinetic energy (J/kg)
l	beam radiation (W/m^2)
P_{r_t}	turbulent Prandtl number
p	pressure (Pa)
P_k	production of turbulent kinetic energy (TKE) due to mean velocity shear
Q	heat (W)
S_m	mass change rate
T	temperature (K)
T_i	fluid inlet temperature (K)
T_o	fluid outlet temperature (K)
S	modulus of the mean rate-of-strain tensor
u_i	velocity component $u, v, \omega\ along x, y, z$, respectively, (m/s)
V	velocity of thermal fluid (m/s)
Greek letter	
δ_{ij}	direction/unit vector ε dissipation of turbulent kinetic energy (J/kg)
η	heat collecting efficiency
μ	dynamic viscosity (Pa·s)
μ_t	turbulent viscosity (Pa·s)
ρ	density (kg/m^3)
σ_k	turbulent Prandtl number for k
σ_ε	turbulent Prandtl number for ε
v	kinematic viscosity (m^2/s)
Abbreviations	
CSC	conical solar collector
SFL	spot Fresnel lens

References

1. Olabi, A.G.; Abdelkareem, M.A. Renewable energy and climate change. *Renew. Sustain. Energy Rev.* **2022**, *158*, 112111. [CrossRef]
2. Renno, C. Characterization of spherical optics performance compared to other types of optical systems in a point-focus CPV system. *Therm. Sci. Eng. Prog.* **2022**, *29*, 101201. [CrossRef]
3. Jensen, A.R.; Sifnaios, I.; Caringal, G.P.; Furbo, S.; Dragsted, J. Thermal performance assessment of the world's first solar thermal Fresnel lens collector field. *Sol. Energy* **2022**, *237*, 447–455. [CrossRef]
4. Ryu, K.; Rhee, J.G.; Park, K.M.; Kim, J. Concept and design of modular Fresnel lenses for concentration solar PV system. *Sol. Energy* **2006**, *80*, 1580–1587. [CrossRef]
5. Han, Y.M.; Wang, R.Z.; Dai, Y.J.; Xiong, A.H. Studies on the light permeance characteristic of a Fresnel lens group applied in high concentration solar energy. *J. Opt. A Pure Appl. Opt.* **2007**, *9*, 988. [CrossRef]
6. Brand, B.; Stambouli, A.B.; Zejli, D. The value of dispatchability of CSP plants in the electricity systems of Morocco and Algeria. *Energy Policy* **2012**, *47*, 321–331. [CrossRef]

7. Ajbar, W.; Parrales, A.; Huicochea, A.; Hernández, J.A. Different ways to improve parabolic trough solar collectors' performance over the last four decades and their applications: A comprehensive review. *Renew. Sustain. Energy Rev.* **2022**, *156*, 111947. [CrossRef]
8. Xie, W.T.; Dai, Y.J.; Wang, R.Z.; Sumathy, K. Concentrated solar energy applications using Fresnel lenses: A review. *Renew. Sustain. Energy Rev.* **2011**, *15*, 2588–2606. [CrossRef]
9. El-Bakry, M.M.; Kassem, M.A.; Hassan, M.A. Passive performance enhancement of parabolic trough solar concentrators using internal radiation heat shields. *Renew. Energy* **2021**, *165*, 52–66. [CrossRef]
10. Xie, W.T.; Dai, Y.J.; Wang, R.Z. Thermal performance analysis of a line-focus Fresnel lens solar collector using different cavity receivers. *Sol. Energy* **2013**, *91*, 242–255. [CrossRef]
11. Lin, M.; Sumathy, K.; Dai, Y.J.; Wang, R.Z.; Chen, Y. Experimental and theoretical analysis on a linear Fresnel reflector solar collector prototype with V-shaped cavity receiver. *Appl. Therm. Eng.* **2013**, *51*, 963–972. [CrossRef]
12. Maurya, A.; Kumar, A.; Sharma, D. A comprehensive review on performance assessment of solar cavity receiver with parabolic dish collector. *Energy Sources Part A Recovery Util. Environ. Eff.* **2022**, *44*, 4808–4845. [CrossRef]
13. Wang, Y.; Liu, Q.; Lei, J.; Jin, H. A three-dimensional simulation of a parabolic trough solar collector system using molten salt as heat transfer fluid. *Appl. Therm. Eng.* **2014**, *70*, 462–476. [CrossRef]
14. Lewandowski, A.; Simms, D. An assessment of linear Fresnel lens concentrators for thermal applications. *Energy* **1987**, *12*, 333–338. [CrossRef]
15. Xie, W.T.; Dai, Y.J.; Wang, R.Z. Numerical and experimental analysis of a point focus solar collector using high concentration imaging PMMA Fresnel lens. *Energy Convers. Manag.* **2011**, *52*, 2417–2426. [CrossRef]
16. Jeter, S.M. Analytical determination of the optical performance of practical parabolic trough collectors from design data. *Sol. Energy* **1987**, *39*, 11–21. [CrossRef]
17. Jeter, S.M. Calculation of the concentrated flux density distribution in parabolic trough collectors by a semifinite formulation. *Sol. Energy* **1986**, *37*, 335–345. [CrossRef]
18. Cheng, Z.D.; He, Y.L.; Cui, F.Q.; Xu, R.J.; Tao, Y.B. Numerical simulation of a parabolic trough solar collector with nonuniform solar flux conditions by coupling FVM and MCRT method. *Sol. Energy* **2012**, *86*, 1770–1784. [CrossRef]
19. Togˇrul, İ.T.; Pehlivan, D. Effect of packing in the airflow passage on the performance of a solar air-heater with conical concentrator. *Appl. Therm. Eng.* **2005**, *25*, 1349–1362. [CrossRef]
20. Padilla, R.V.; Demirkaya, G.; Goswami, D.Y.; Stefanakos, E.; Rahman, M.M. Heat transfer analysis of parabolic trough solar receiver. *Appl. Energy* **2011**, *88*, 5097–5110. [CrossRef]
21. Alsalame, H.A.M.; Hussain, M.I.; Amjad, W.; Ali, A.; Lee, G.H. Thermo-economic performance evaluation of a conical solar concentrating system using coil-based absorber. *Energies* **2022**, *15*, 3369. [CrossRef]
22. El-Refaie, M.F. Theoretical analysis of the performance of a conical solar concentrator. *Appl. Energy* **1982**, *12*, 37–51. [CrossRef]
23. Natarajan, S.K.; Mallick, T.K.; Katz, M.; Weingaertner, S. Numerical investigations of solar cell temperature for photovoltaic concentrator system with and without passive cooling arrangements. *Int. J. Therm. Sci.* **2011**, *50*, 2514–2521. [CrossRef]
24. Mahmood Alsalame, H.A.; Lee, J.H.; Lee, G.H. Performance Evaluation of a Photovoltaic Thermal (PVT) system using nanofluids. *Energies* **2021**, *14*, 301. [CrossRef]
25. Hussain, M.I.; Lee, G.H. Numerical and experimental heat transfer analyses of a novel concentric tube absorber under non-uniform solar flux condition. *Renew. Energy* **2017**, *103*, 49–57. [CrossRef]
26. Engineering Toolbox. (n.d.). Convective Heat Transfer. Available online: https://www.engineeringtoolbox.com/convective-heat-transfer-d_430.html (accessed on 8 October 2024).
27. Abdelrazik, A.S.; Osama, A.; Allam, A.N.; Shboul, B.; Sharafeldin, M.A.; Elwardany, M.; Masoud, A.M. ANSYS-Fluent numerical modeling of the solar thermal and hybrid photovoltaic-based solar harvesting systems. *J. Therm. Anal. Calorim.* **2023**, *148*, 11373–11424. [CrossRef]
28. Andersson, B.; Andersson, R.; Håkansson, L.; Mortensen, M.; Sudiyo, R.; Van Wachem, B. *Computational Fluid Dynamics for Engineers*; Cambridge University Press: Cambridge, UK, 2011.
29. Versteeg, H.K. *An Introduction to Computational Fluid Dynamics the Finite Volume Method, 2/E*; Pearson Education India: Bengaluru, India, 2007.

Disclaimer/Publisher's Note: The statements, opinions and data contained in all publications are solely those of the individual author(s) and contributor(s) and not of MDPI and/or the editor(s). MDPI and/or the editor(s) disclaim responsibility for any injury to people or property resulting from any ideas, methods, instructions or products referred to in the content.